

Non-neutral plasma manipulation techniques in development of a high-capacity positron trap

Cite as: Rev. Sci. Instrum. 92, 123504 (2021); doi: 10.1063/5.0067666

Submitted: 18 August 2021 • Accepted: 9 November 2021 •

Published Online: 2 December 2021



View Online



Export Citation



CrossMark

M. Singer,^{1,2,a)}  S. König,²  M. R. Stoneking,^{3,4}  P. Steinbrunner,¹ J. R. Danielson,⁵  L. Schweikhard,²
and T. Sunn Pedersen^{1,2} 

AFFILIATIONS

¹Max-Planck Institute for Plasma Physics, 17491 Greifswald, Germany

²University of Greifswald, 17489 Greifswald, Germany

³Max-Planck Institute for Plasma Physics, 85748 Garching, Germany

⁴Lawrence University, Appleton, Wisconsin 54911, USA

⁵University of California, San Diego, La Jolla, California 92093, USA

^{a)}Author to whom correspondence should be addressed: martin.singer@ipp.mpg.de

ABSTRACT

Preliminary experiments have been performed toward the development of a multi-cell Penning–Malmberg trap for the storage of large numbers of positrons ($\geq 10^{10}e^+$). We introduce the master-cell test trap and the diagnostic tools for first experiments with electrons. The usage of a phosphor screen to measure the z-integrated plasma distribution and the number of confined particles is demonstrated, as well as the trap alignment to the magnetic field ($B = 3.1$ T) using the $m = 1$ diocotron mode. The plasma parameters and expansion are described along with the autoresonant excitation of the diocotron mode using rotating dipole fields and frequency chirped sinusoidal drive signals. We analyze the reproducibility of the excitation and use these findings to settle on the path for the next generation multi-cell test device.

© 2021 Author(s). All article content, except where otherwise noted, is licensed under a Creative Commons Attribution (CC BY) license (<http://creativecommons.org/licenses/by/4.0/>). <https://doi.org/10.1063/5.0067666>

I. INTRODUCTION

Positrons are one of the rarest and most expensive substances on Earth. As a glimpse into the nature of antimatter, they are in themselves interesting objects to study, but they can also be used for many different experiments including material surface studies¹ and the formation of anti-hydrogen² to test the charge, parity, and time (CPT) reversal symmetry theorem (CPT)-theorem or the gravitational response of antimatter,³ as well as to investigate fundamental plasma physics. The latter is the focus of the “A Positron Electron eXperiment” (APEX) collaboration. Our goal is the formation of a magnetized positron–electron plasma at low temperatures and sufficiently high densities, with a spatial extent of several Debye lengths to study collective behavior and test the fundamental behavior of mass-symmetric neutral plasmas.^{4–6}

To achieve this goal, 10^{10} – 10^{11} cold (~ 1 eV) positrons are needed. Currently, the records for the largest number of positrons are $3.8 \cdot 10^8$ accumulated over 9.3 min,⁷ $1.2 \cdot 10^9$ over 2.5 h,⁸ and $4.0 \cdot 10^9$ over 4.5 h.⁹ All of these experiments use

Penning–Malmberg (PM) traps in which non-neutral plasmas are confined axially due to electrical potentials and radially due to a strong, uniform magnetic field in the axial direction.¹⁰ In the first stage of these schemes, positrons from a continuous source are cooled and accumulated in a buffer-gas trap. In the second stage, they are transferred and further accumulated in a high magnetic field trap. While the efficiency of the first stage has been improved over the years, the limitations on the total number of positrons that can be accumulated with this approach lie in the second stage. If the number of positrons accumulated in a PM trap increases, a corresponding space-charge potential builds up that has its maximum on the symmetry axis. Assuming a long (compared to its radius), evenly distributed cylindrical positron plasma, the on-axis potential has the form¹⁰

$$|\phi_P(r=0)| = \frac{|e|N}{4\pi\epsilon_0 l_P} \left(1 + 2 \ln \left(\frac{r_W}{r_P} \right) \right), \quad (1)$$

where $|e|N$ is the accumulated charge, l_P is the plasma length, r_P is the plasma radius, and r_W is the inner wall radius of the trap electrodes.

To confine such a plasma in a PM trap, the applied confinement potentials on axis $\phi_C(r=0)$ have to be larger than the plasma space-charge potential, i.e., $|\phi_C(r=0)| > |\phi_p(r=0)|$. This means that, for a fixed plasma length and increasing particle number, the necessary confinement potentials become large. Our goal is to accumulate and confine large numbers of particles, thereby reaching a high overall plasma space-charge. This usually implies high confinement potentials and the use of kV plugging potentials.

The use of high voltage can be avoided by separating the plasma into multiple PM traps or “storage-cells.” Using a honeycomb-like arrangement, it is possible to fit multiple storage-cells in a small volume, with each of them carrying a portion of the overall space-charge. Surko and Greaves first suggested and developed this multi-cell trap concept.¹¹ Later, Danielson *et al.* introduced the idea of first confining the plasma in a large diameter “master-cell” trap, and then moving the plasma off-axis and axially transferring it into the storage-cells, in which multiple pulses are accumulated and stored until the desired number of positrons integrated over all cells is reached.¹² Many of the techniques needed to perform these manipulations have been demonstrated.^{12–15} Two key challenges resulting from the UCSD experiments were the critical need to have a good alignment procedure for the electrodes and the need to develop efficient autoresonance control that minimizes expansion. The work reported here addresses these challenges.

The APEX collaboration aims to continue the development of this multi-cell concept for the accumulation of large positron (e^+) numbers. Considering that 10^{10} – $10^{11}e^+$ are needed for a positron–electron plasma and that a buffer-gas trap will be utilized to deliver pulses of $\sim 2 \cdot 10^8e^+$ every minute with a high transfer efficiency, it will take between 5 min and 8 h to accumulate the required number of positrons. Great care must, therefore, be taken to optimize the plasma confinement in each storage-cell in terms of the particle loss and radial expansion, to ensure that the plasma stays confined over the long accumulation period. After accumulating the desired number of positrons, they will be transferred from the storage-cells back into the master-cell and delivered to the pair-plasma experiment. Here, we describe preliminary experiments that have been performed at the Max Planck Institute for Plasma Physics with a master-cell test trap as the first step toward constructing a new multi-cell trap. In particular, we describe the use of a technique for alignment of the electrodes suitable for the multi-cell trap and report a unique mode of operation of the autoresonance excitation that shows solid performance. Section II introduces the experimental setup, its diagnostics, and a typical experimental cycle. Section III discusses a robust technique for the alignment of the trap electrodes to the magnetic field. The typical plasma parameters and the confinement achieved so far are given in Sec. IV, followed by a description of a new operating mode of autoresonant excitation of the $m = 1$ diocotron mode suitable for use in filling off-axis traps in Sec. V. Section VI outlines the next steps needed to begin multi-cell trap operation.

II. EXPERIMENTAL SETUP

The present experiments were performed with electrons in the master-cell test trap, a Penning–Malmberg trap that is embedded in a uniform magnetic field of $B_0 = 3.114(2)$ T provided by a superconducting magnet. A scaled schematic of the trap structure is shown in

Fig. 1, along with a plot of the on-axis magnetic field and the on-axis vacuum potential profile, i.e., the potential profile due to the applied voltages on the electrodes. Two cryogenic pumps, one at each side of the experimental chamber, bring the background pressure to about $1 \cdot 10^{-9}$ mbar as measured with ionization gauges ~ 1.4 m away from the experimental region where the stray magnetic field is low enough to operate the gauges.

The master-cell trap consists of ten cylindrical electrodes (denoted as E1–E10 in Fig. 1) with an inner wall radius of $r_W = 37$ mm and a gap of 0.5 mm between each other, to which individual potentials can be applied. The wall radius was chosen according to the size of the final multi-cell device (≈ 37 mm), given the bore radius of the magnet (67.5 mm). The two end electrodes (E1 and E10) have a length of 60 mm and the eight inner ones (E2–E9) are 40 mm long. Four electrodes are segmented, two into eight segments (E2 and E9) and two into four segments (E3 and E8). These are used for plasma diagnostics and manipulation. All electrodes are made of aluminum coated with colloidal graphite (diluted in isopropanol and applied using an air brush). Several previous studies have demonstrated that the use of colloidal graphite instead of gold plating can help reduce surface potential variations and lead to improved lifetime.^{16,17} The electrodes are clamped together with insulating spacers made of polyether ether ketone (PEEK).

For the present experiments, typical confinement potentials of $\phi_{C,1} = -200$ V are applied to an upstream electrode and $\phi_{C,2} = -300$ V to a downstream one. Vacuum solutions to Laplace’s equation yield a confinement potential of ~ -120 V on the axis (see Fig. 1). The electron source is a linear filament made of rhenium with a typical emission current in the microampere range. All present experiments were performed with electrons. For the ultimate application with positrons, only the sign of the charge and potentials has to be changed. The emitter is biased to -20 V to accelerate electrons into the trap. An aperture placed in front of the source (not included in Fig. 1) can be switched between potentials to either let the electrons pass or block them from streaming into the trap during the appropriate phases of the experimental sequence.

The experiments are performed in fill–hold–manipulate–dump cycles. These are controlled using a Pulsed–Pattern Generator (PPG) that is based on a Field Programmable Gate Array (FPGA) that allows precise and reproducible timing down to the nanosecond range for the measurement procedures.¹⁸ In the first (“fill”) step of the cycle, the aperture and upstream electrode are grounded while the confinement potential is applied to an electrode at the downstream side. Electrons stream into the trap, are reflected at the downstream electrode, and stream back into the direction of the emitter. Due to two-stream-instabilities,¹⁹ an equilibrium electron distribution eventually forms between the emitter and the downstream electrode after 0.8–1 ms. In the second (“hold”) step, the potential at the upstream confinement electrode is brought to -200 V, trapping electrons in the confinement volume. Simultaneously, the potential on the aperture of the electron source is brought to -300 V, preventing further electrons from streaming into the trap. By using different trapping electrodes, the length of the plasma can be varied as well as the number of confined particles. In the third step, the plasma is confined in the trap and can be manipulated, diagnosed, or simply held for a predetermined amount of time.

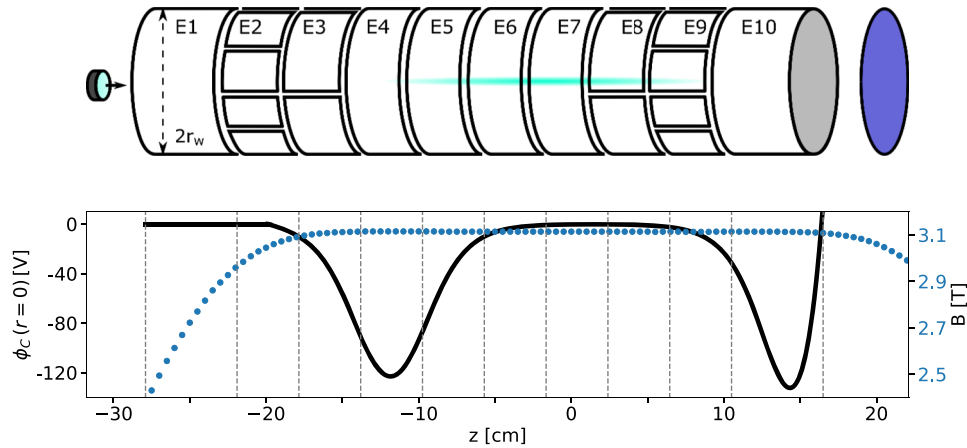


FIG. 1. The upper schematic shows the experimental setup with the electron emitter on the left (upstream) side, the trap electrodes with their respective labels in the middle, and the phosphor screen on the right (downstream) side. The dashed line on the upstream side represents the trap diameter. In the bottom graph, the magnetic field on the axis (blue dots) as well as the on-axis vacuum potential for applied potentials of $\phi_{c,1} = -200$ V at E4, $\phi_{c,2} = -300$ V at E10, and 5 kV at the screen (black line) are visualized. The vertical gray dashed lines represent the locations of the gaps between electrodes along the z -axis and $z = 0$ is chosen to lie in the center of the homogeneous magnetic field region.

Since the electron emitter is slightly displaced relative to the trap axis of symmetry, a residual $m = 1$ diocotron mode of the plasma arises. In Sec. III, we show how this feature can be used to align the trap wall parallel to the background magnetic field. However, for most experiments, this residual diocotron mode is unwanted and hence must be damped. To this end, a feedback-damping²⁰ circuit is employed, which takes the image-charge signal from one sector of a segmented electrode, amplifies it, and applies it to the sector that is 180° displaced. This damping scheme is shown in Fig. 2, as well as an experimental example of the plasma displacement during the damping process. The displacement is derived from the radial plasma position, the measurement of which is described in the next two paragraphs. By careful adjustment of the phase shift of the amplified signal, and after applying an exponential fit to the measurement (solid black line in Fig. 2), we find that the residual diocotron mode is damped below 1% of its initial amplitude after 480 ms.

In the last (“dump”) step, the confinement potential at the downstream electrode is set to 0 V so that the plasma is released and can be diagnosed. It is dumped onto a phosphor screen located ~ 3 cm downstream from the trap, which is biased to +5 kV. This screen is a commercial glass coated with indium-tin-oxide onto which we have deposited by a sedimentation technique²¹ a layer of the phosphor P22b Sn:ZnAg. Particles with a sufficient kinetic energy²² that strike this material cause it to fluoresce. The z -integrated plasma distribution as well as the position of the plasma in the trap at the time of the dump are imaged with a Complementary Metal-Oxide-Semiconductor (CMOS) camera with a depth of 12 bits.

To obtain the plasma position and radius, the integrated plasma distribution is assumed to be circularly symmetric and a variant of a 2D super-Gaussian function

$$f(x, y) = a \cdot \exp\left(-\left(\frac{\sqrt{(x - x_0)^2 + (y - y_0)^2}}{r_p}\right)^n\right) + c \quad (2)$$

is fitted to the data. Here, x_0 and y_0 denote the plasma position, i.e., the position of the maximum brightness in the xy -plane, a is its intensity, c is an offset, and n is the power in the argument of the exponential function. We define the plasma radius r_p as the location at which the super-Gaussian function falls off to $1/e \approx 0.368$ of its maximum value. An example of such a plasma image is shown in Fig. 3, along with x - and y -slices through the center showing the fit to the super-Gaussian profile for these data. Here, along both slices, the fit yields $r_p = 1.2$ mm and $n = 1.9$, showing that this plasma is close to a Gaussian shape. Since the screen is in a lower magnetic field ($B_{\text{Screen}} = 2.965$ T) compared to the confinement volume, the plasma

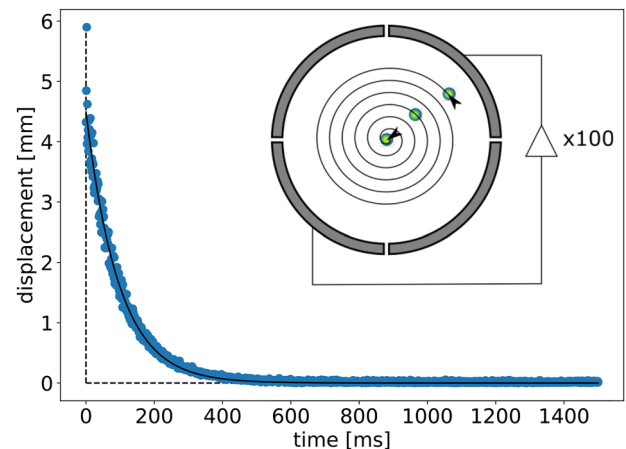


FIG. 2. Feedback-damping of the residual diocotron mode. The inset shows schematically how the image-charge signal is picked up at one sector, amplified, phase-shifted, and applied to the opposing sector. The graph shows the measured displacement of the plasma as a function of time while the feedback damping is applied. An exponential decay fit (solid black line) yields a damping of the residual diocotron mode below 1% of its initial amplitude after 480 ms.

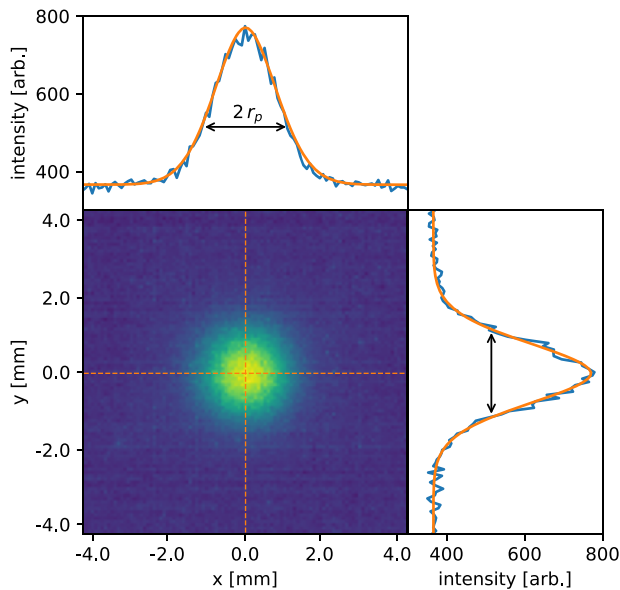


FIG. 3. Image of the z -integrated plasma distribution measured at the phosphor screen. The central image shows a magnified view of the central plasma region. The graphs on the top and on the right show horizontal (top) and vertical (right) cuts through the center of the image with a width of one pixel in blue. They are represented by the dashed orange lines in the central image and used to fit a 2D super-Gaussian distribution function (orange solid line) as well as to obtain the plasma radius. The fit yields $r_p = 1.2$ mm and $n = 1.9$.

image is slightly magnified. This has been taken into account using conservation of the magnetic flux and measurements of the on-axis magnetic field (Fig. 1). This calibration leads to a scaling factor of $\kappa = \sqrt{B_0/B_{\text{Screen}}} \approx 1.025$. The screen can also be used to measure the

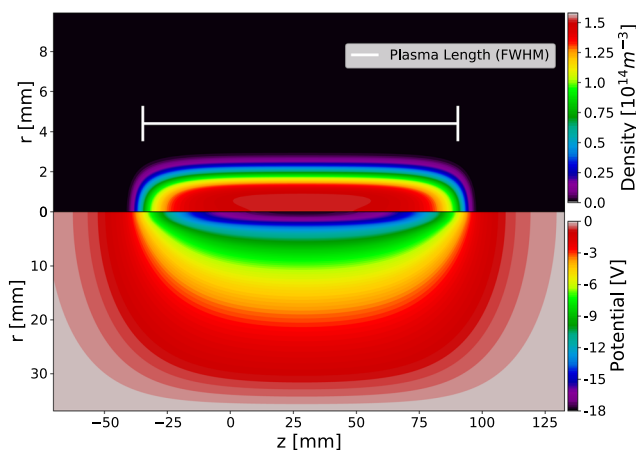


FIG. 4. Poisson-Boltzmann solution for a typical electron plasma confined between the electrodes E4 (at -200 V) and E10 (at -300 V), with E5–E9 grounded. The top graph shows the density distribution, which is used to determine the plasma length (white line). The lower graph shows the potential, which is due to the plasma space charge. The plasma parameters are $N = 2 \cdot 10^8$, $r_p = 2$ mm and $n = 4$, which gives a central density of $1.5 \cdot 10^{14} \text{ m}^{-3}$, an on-axis length of $l_p = 125$ mm, and potential $\phi_p(r=0) = -18$ V.

total number of confined particles N when used as a charge collector that is biased to $+200$ V and using a charge-integrating circuit (CREMAT CR-113). Since the plasma profile and particle number are measured and the geometry and applied potential are well known, a Poisson–Boltzmann solver can be used to solve for the local thermal equilibrium distribution of the confined plasma and to obtain the plasma length l_p .²³ Figure 4 shows a solution of the plasma distribution in the trap that is used to obtain information on the space-charge potential and the length of the plasma, defined as the full width at half maximum (FWHM) of the axial plasma elongation.

III. ALIGNING THE TRAP WITH THE MAGNETIC FIELD

Accurate alignment of the trap axis to the magnetic field is crucial for good confinement of non-neutral plasmas in a Penning–Malmberg trap. To change the alignment of the trap, which is embedded into the bore of the superconducting magnet, six screws on each side of the vacuum tube can be used to adjust the horizontal and vertical position of the tube with respect to the field. One way to adjust this positioning is to measure the plasma expansion or charge decay. If the alignment is poor, the plasma expands quickly compared to a well-aligned situation. However, these measurements can become quite time consuming, reaching a regime where a visible expansion can be measured only after 100 s or longer. Hence, an alignment procedure has been adapted that compares the motion of the $m = 1$ diocotron mode in different axial positions of the trap, a technique developed by Aoki *et al.*²⁴

The procedure makes use of the fact that the electron emitter is offset from the symmetry axis of the trap by a small amount. This leads to a residual $m = 1$ diocotron mode when the plasma is confined. Since the particles and the initial electron column follow the magnetic field lines from the source, the amplitude of the diocotron motion varies at different distances from the source when there is a misalignment of the magnetic field to the electrode wall, i.e., when they are not parallel to each other. This is shown schematically in Fig. 5, demonstrating how electrons following the magnetic field lines from the source (green) will perform different diocotron motions in two confinement volumes (CV1 in red and CV2 in blue) due to the misalignment to the magnetic field, and how these motions will appear on the phosphor screen. By imaging the residual diocotron motion around the trap axis in two different regions of the trap on the phosphor screen, we can quantify the misalignment of the wall to the magnetic field and also determine the direction the trap must be shifted to be aligned with the magnetic field.

We performed fill–hold–dump measurements in two different confinement volumes of the same length and a relative distance of 28.35 cm from each other, one close to the electron emitter (CV1 in Fig. 5) and the other closer to the screen (CV2). For each measurement, the hold time was increased in small steps of $5 \mu\text{s}$ until two cycles of the diocotron motion around the trap center are imaged. Circles were fitted to the data to determine their centers and the distance ΔC between the centers of each circle gives a measure of the misalignment and the direction in which the traps needs to be adjusted. In Fig. 6(a), the residual diocotron motion was monitored before the alignment and the observed ΔC corresponds to an initial misalignment of $\sim 0.141(15)^\circ$. The arrow indicates in which

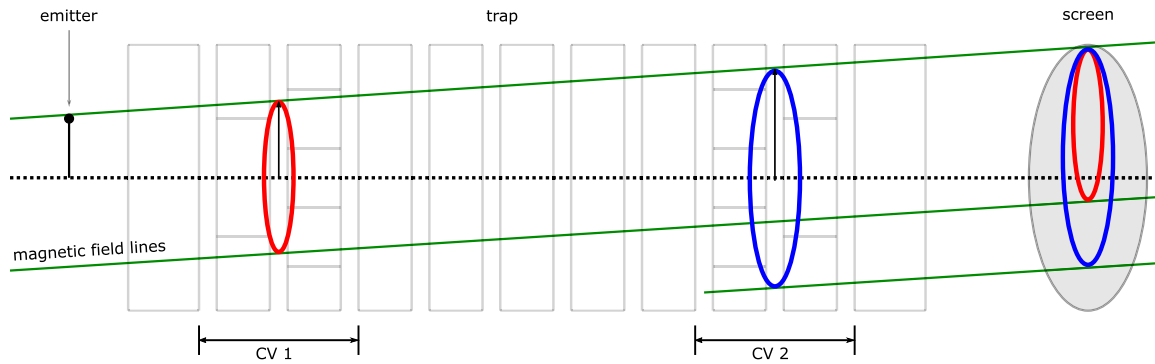


FIG. 5. Schematic for the alignment procedure, adapted from Aoki *et al.*,²⁴ with the emitter on the left, the trap in the middle, and the screen on the right side. The location of confinement volume 1 (CV1) and confinement volume 2 (CV2) are marked below. The diocotron trajectories in each confinement volume and their images on the screen are represented in red (CV1) and blue (CV2), respectively. Reproduced with permission from Aoki *et al.*, Jpn. J. Appl. Phys., Part 1 **43**, 7777 (2004). Copyright 2004 IOP Publishing.

direction the side of CV1 has to be shifted. After the position has been shifted accordingly, the measurement and correction of the alignment were repeated multiple times [Figs. 6(b)–6(d)]. With this technique, the trap was aligned until the difference between the centers reached $\Delta C = 60(77) \mu\text{m}$, which corresponds to an angular misalignment of $\sim 0.012(12)^\circ$. This value lies within the range of the uncertainty of this procedure, which is limited due to our shot-to-shot reproducibility.

As has been discussed,¹⁵ accurate alignment of the storage cells is critical in the success of the multi-cell trap concept. The future

multi-cell trap will have the ability to independently adjust the storage cell alignment, and thus, a reliable method of measuring small misalignments is necessary. Here, we have demonstrated the use of well controlled diocotron modes to measure the alignment with the precision necessary for the multi-cell trap.

IV. PLASMA PARAMETERS, CONFINEMENT, AND EXPANSION

In this section, the typical plasma parameters are described, which are achieved after aligning the trap to the magnetic field using a fill- and preparation routine including the damping of the residual diocotron motion. In this section and in Sec. V, we focus solely on plasmas confined between E4, E5, E6 or E7 to E10 because of the homogeneity of the magnetic field in these regions (see Fig. 1).

Given the preparation described above, plasmas with initial electron numbers from $N = 0.5 \cdot 10^8$ to $2 \cdot 10^8$ are confined with a shot-to-shot reproducibility of $\Delta N/N \approx 2\%$, plasma radii from $r_p = 0.5$ to 1 mm, and lengths from $l_p = 50$ to 125 mm. If a cylindrical plasma shape is assumed, these plasmas have an on-axis space charge potential of $\phi_p(r=0) \geq -19$ V. Since the plasma temperatures are less than 10 eV and the on-axis confinement potential is $\phi_C = -120$ V, these plasmas are well confined. Measurements of the axial plasma temperature^{25,26} yield an initial plasma temperature of 0.5–1 eV on the axis. Given the average density of $n_0 = 5 \cdot 10^{14} \text{ m}^{-3}$, the initial Debye length is about 0.2–0.3 mm. Therefore, the conditions $r_p > \lambda_D$ and $l_p \gg \lambda_D$ are satisfied and the charged cloud qualifies as a non-neutral plasma.

The plasma expansion was measured without any further manipulation. Repeated fill–hold–dump cycles with increasing holding times up to 1000 s after the damping of the residual diocotron mode were performed. For each cycle, the plasma profile and the number of confined electrons were measured. An example of such a measurement is shown in Fig. 7. Plotted vs the holding time, it shows the mean plasma density n_0 in the first panel, the super-Gaussian exponent n in the second, the plasma radius r_p in the third, and the number of confined particles N in the fourth. For holding times up to 2 s, all of these parameters remain constant. Later, we see that

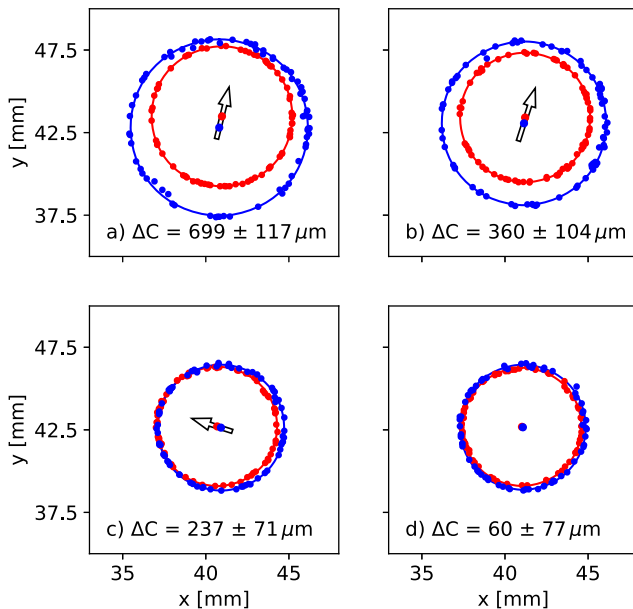


FIG. 6. Measured diocotron mode trajectories in two different confinement volumes, CV1 upstream (red) and CV2 downstream (blue), and their center distance ΔC for four different stages of the alignment procedure: (a) before the alignment, (b) and (c), two intermediate steps, and (d) the final measurement after optimizing the alignment.

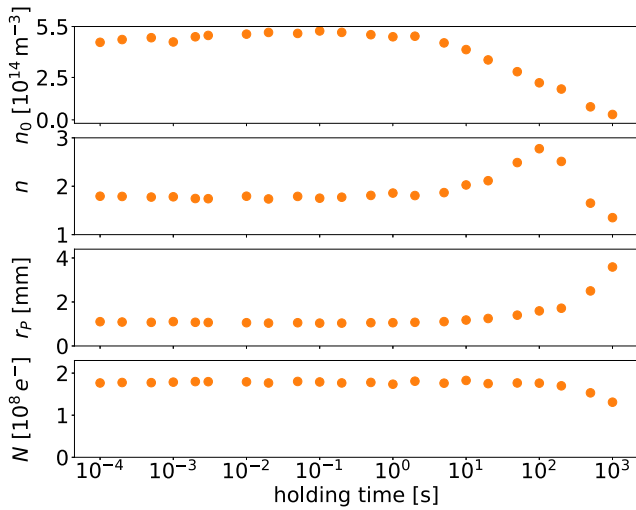


FIG. 7. Measurement of the plasma expansion for the confinement between E5 (at -200 V) and E10 (at -300 V), which corresponds to $l_p = 101$ mm. The first panel shows the evolution of the mean plasma density n_0 over the holding time. The second panel shows the evolution of the super-Gaussian exponent n . The third and fourth panels show the evolution of the plasma radius r_p and of the number of trapped particles N , respectively.

the density decreases while the super-Gaussian exponent and the radius increase. This indicates that the plasma expands and changes its shape from a sharply peaked profile ($n < 2$) to a Gaussian-shape ($n = 2$), eventually becoming a flat-top profile ($n > 2$). Starting at ~ 100 s, the plasma loses particles while further expanding, becoming less and less dense. While the plasma further expands, it appears to evolve back to a peaked profile, given the decreasing value of the parameter n . However, this is a consequence of the fit failing to adequately determine the profile for these diffuse plasma cases. Figure 8 shows a visualization of this. It shows two 2D profiles from the data in Fig. 7, one at 100 s and one at 500 s on the left and right side, respectively. The dashed line in the lower images shows the cut through each of those images along which the profiles shown in the upper panels, with super-Gaussian fits, are taken. For the left image, the fitted function yields a flat-top profile ($n = 3.01$) and represents the overall shape of the 2D profile well, while for the right image, the fit finds a spot-like ($n = 1.84$) profile. The latter does not represent the 2D distribution in all its detail because, for long holding times, the profiles develop a distinctive low-density halo around the plasma center. To adequately represent these profiles, at least two different super-Gaussian functions would be needed: one for the central plasma and one for the low density halo. This becomes important if we are looking at the radial plasma transport in more detail and has to be accounted for in future studies, but, since the simple 2D super-Gaussian distribution is a good measure for the overall plasma radius and only fails at long holding times, we use it here to describe the plasma radius.

The results of further holding time measurements for different plasma lengths are shown in Fig. 9, where the plasma radius and the number of confined particles are plotted vs the holding time. Over the course of the trapping time, the plasma slowly expands up to 4 mm. After this time, it was not possible to measure the profile since

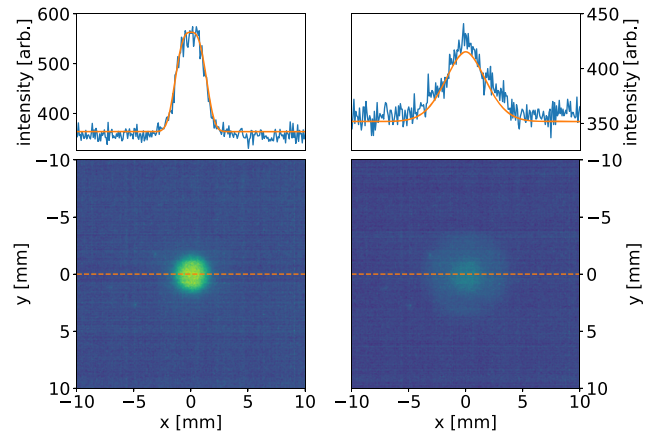


FIG. 8. Two 2D plasma profiles from the data of Fig. 7. The left shows the measured plasma profile after 100 s and the right after 500 s. The graphs on the top show the center x -plane with a width of one pixel, which are represented by the dashed orange line in the image below. These graphs show the results of the fitted 2D super-Gaussian distribution to both cases, which yield a fit-parameter $n = 3.01$ for the 100 s and $n = 1.84$ for the 500 s case.

it became too diffuse to be imaged with our current diagnostic due to the stray light emitted from the emitter. For lengths of 51 and 76 mm, this is the case even at 500 and 1000 s, respectively. The particle loss is clearly measurable after holding times ≥ 100 s. After this time, the number slowly decreases until at 1000 s $\sim 25\%$ of the initial particles have been lost. This behavior seems to be independent of the plasma length even though the number of confined particles is different for each length. This observation is at odds with other experiments that have measured an expansion rate for a non-neutral plasma in a PM trap that is proportional to the square of the plasma length.^{27,28}

Since the plasmas described here are well confined (meaning on axis $|\phi_p| \ll |\phi_C|$ is fulfilled, and the temperature is relatively low), it should not be possible for particles to escape the trap axially due to

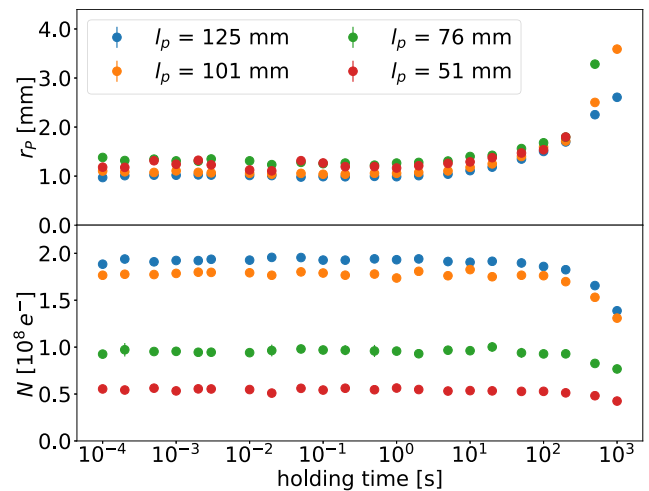


FIG. 9. Evolution of the plasma radius (top) and the number of trapped electrons (lower panel) vs the holding time, for several plasma lengths (see the color code).

expansion and the associated heating¹⁰ of the plasma. In addition, over the course of the holding time, the main plasma body expands to radii that remain much smaller than the wall radius ($r_p \ll r_w$) so that the particles in the main plasma region should not be lost radially on the surface of the electrodes. We, therefore, speculate that there is a low density halo of electrons surrounding the main plasma body. This halo may originate in the complicated plasma formation process and particles may be lost from this halo radially before those of the main plasma. With our current diagnostics, it was not possible to observe this halo, but it may be the reason why no significant difference in the expansion for different plasma lengths was observed. Another possibility is that the heated cathode forms excited hydrogen molecules, and these dissociatively attach to the plasma electrons forming H^- .²⁹ These particles would not be observed, and thus, it would appear as a loss of particles to our diagnostics.

V. AUTORESONANT EXCITATION OF THE DIOCOTRON MODE

It has been shown that the $m = 1$ diocotron mode can be excited in a controlled manner for a non-neutral plasma in a Penning–Malmberg trap³⁰ and that this mode can be used to address off-axis storage-cells.^{14,15} Indeed, for the addressing of the off-axis cells of a multi-cell trap, the control over the radial positioning of the plasma is crucial. Due to spatial constraints, we aim to place the off-axis cells at $\sim 70\%$ of the wall radius of the master-cell. In this section, we demonstrate the control of this motion in our trap and show that this is a suitable displacement for the storage-cells in the next multi-cell trap.

In contrast to previous work on autoresonant excitation, which only used a single segment of the conducting wall,^{14,15,30} the experiments here use a variant of this technique. We found that the excitation of the diocotron motion in our trap is highly reproducible using a rotating dipole field where a chirped sinusoidal signal is applied to the fourfold segmented electrode E8 with a phase shift of 90° between neighboring segments, meaning 0° at the first, 90° at the second, 180° at the third, and 270° at the fourth segment. One example is shown in Fig. 10 where the frequency was chirped from 1 to 320 Hz with a chirp rate of 2 kHz/s at an amplitude of $4V_{pp}$. It shows the off-axis displacement as a fraction of the wall radius (blue dots) and the corresponding plasma radius (orange dots) for plasmas that are dumped onto the screen for increasing excitation times. It is possible to stably excite the plasma up to $D/r_w = 0.92$, i.e., 92% of the wall radius. During excitation of the diocotron mode, the plasma expands. However, up to a displacement of 70%, this expansion is small compared to the initial plasma radius (solid black lines).

The dashed line in Fig. 10 shows the displacement vs time predicted by matching the drive frequency to the non-linear diocotron frequency ω_{NL} given by the following formula:³⁰

$$\omega_{NL} = \omega_0 \frac{1}{1 - D^2/r_w^2}, \quad (3)$$

where $\omega_0 = eN/2\pi\epsilon_0 I_p B r_w$ is the small amplitude or linear diocotron frequency. The linear frequency was estimated to be 125 Hz, which matches approximately the time where the autoresonant drive couples strongly to the diocotron motion and mode growth accelerates.

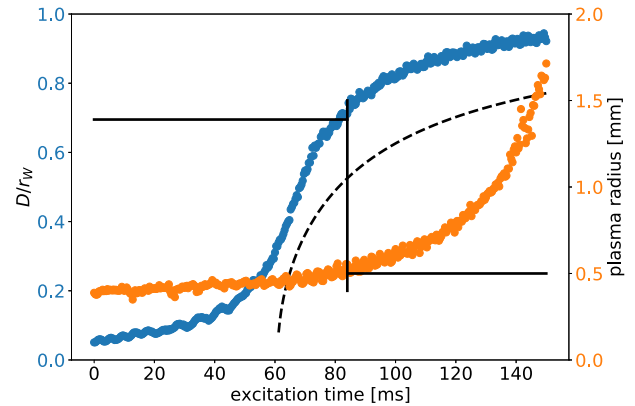


FIG. 10. Diocotron mode off-axis displacement (as a fraction of the wall radius $r_w = 37$ mm blue line) and the corresponding plasma radius (orange line) as a function of the autoresonant excitation time where a sinusoidal frequency signal with an amplitude of $4V_{pp}$ was chirped at a rate of 2 kHz/s. The solid black line marks the time and related plasma radius when the plasma is displaced to 70% of the wall radius. The dashed black line shows the evolution of the plasma displacement predicted by Eq. (3).

The prediction matches the observation for the displacement reasonably well except for an initial offset. Not all non-linearities in the $m = 1$ mode frequency are captured by Eq. (3), so a precise match is not expected. Additional considerations that affect the mode frequency at high amplitude include the elliptical distortion of the plasma cross-section when it approaches the wall³¹ and the finite axial extent of the plasma.^{32,33} For our purposes, it is not necessary to identify these effects as long as we can reproducibly excite the mode to a controlled amplitude.

The measurement in Fig. 10 is comprised of 376 fill–hold–dump cycles. These data, therefore, show that this excitation scheme is fairly reproducible. However, to determine whether it is reasonable to place the center of the off-axis cells at a displacement of 70%, it is crucial to confirm that it is possible to reproducibly address not only a determined radius but also a well-defined phase (i.e., azimuthal position). To further test the reproducibility of the off-axis displacement, the mode is excited 50 times and at each measurement, the plasma is dumped after an excitation time of 80 ms, which corresponds to 68% of the wall radius. If the excitation is phase-locked to the diocotron motion, it should be possible to dump the plasma at a reproducible radius and an azimuthal angle. The outcome of these measurements is shown in Fig. 11. The blue dots mark the center of the dumped plasmas, the dashed line represents $D/r_w = 0.68$, and the solid line represents a hypothetical storage-cell with a wall radius of 6 mm with its center on the dashed line. One can see that all the blue dots are quite near the dashed line. In the enlarged view of the region in the upper right of Fig. 11, one can see that the scatter in the plasma position is about 1 mm horizontally and less than 0.5 mm vertically. This scatter is probably due to the shot-to-shot variation in the electron number as well as a small amplitude sloshing motion of the electron plasma in the well of the exciting field.¹⁴ Compared to the plasma radius after the excitation ($r_p = 0.5$ mm, the blue dotted line in the enlarged view), the scatter is small. It is also small compared to the size of the prospective storage-cell wall radius of 6 mm. Therefore,

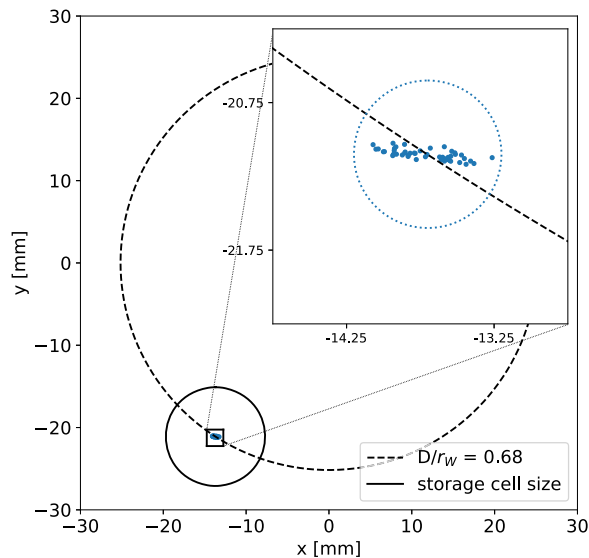


FIG. 11. Reproducibility of the diocotron excitation up to $D/r_w = 0.68$. The dashed line marks 68% of the wall radius. The inset square expands the region in which the plasma has been dumped for the 50 measurements. The solid black circle represents the prospective size of a storage-cell with a diameter of 12 mm. The blue dotted line in the inset represents the typical size of the plasma after the excitation with $r_p = 0.5$ mm.

we determined that the off-axis storage-cells for a future multi-cell trap can be placed at $\sim D/r_w = 0.7$ compared to the master-cell.

Reproducible excitation up to large fractions of the wall radius with negligible plasma expansion is, as discussed above, critical for the development of the multi-cell concept. We have shown here that, using the chirped dipole drive technique, we can reproducibly move particles out to 70% of the wall radius with minimal expansion, a result that gives us confidence in proceeding to tests with off-axis storage cells.

VI. TOWARD A MULTI-CELL TRAP

Based on the present results, a multi-cell test trap has been designed and is being assembled. It has one on-axis cell and two off-axis cells with their centers at 70% of the master-cell's wall radius. Due to the radial spatial limitations in our current vacuum setup, the wall radius of the storage-cells was chosen to be 6 mm. The prototype multi-cell trap can be extended, without major redesign, to seven storage-cells. Each storage-cell is expected to confine up to $4 \cdot 10^9 e$, so the prototype will be able to accumulate approximately up to $2 \cdot 10^{10}$ particles. The design is made modular so that the multi-cell trap can eventually be extended to 14 or 21 cells to reach 10^{11} particles.

The next experiments will test the transfer of plasma into the off-axis cells as well as the simultaneous confinement in multiple cells. The rotating wall technique^{27,28} will be applied in the master- and storage-cells. We plan to address the question whether a simultaneous, in-phase (or feed-forward) application of the rotating wall signal is possible or whether separately phased (feedback) compression signals need to be applied to each cell individually. We anticipate being able to confine particles for 50 min or more, as needed to

eventually accumulate the target number of positrons for the APEX experiments. Finally, we want to study the process required to dump plasmas from the off-axis cells and how the many positrons could be provided to our positron–electron plasma confinement devices using such a system.

Diagnostic capabilities will be improved with a commercial phosphor screen that is coated with P43 phosphor, the luminescence of which better matches the CMOS camera quantum efficiency, and that will be operated at higher potentials, up to 8 kV. The electron emitter will be upgraded with a lanthanum-hexaboride (LaB_6) crystal with a lower work function of 2.6–2.8 eV³⁴ so that sufficient electron current can be emitted at lower temperature, thereby producing less stray light. This should result in a much improved imaging quality and may, therefore, allow for a better diagnosis of the plasma, and, for example, the detection of the aforementioned halo.

VII. SUMMARY

We presented the design and initial operation of a master-cell Penning–Malmberg trap setup, which will be part of the next multi-cell trap for high capacity positron storage. Experiments reported here used electrons instead of positrons. Specifically, we demonstrated a highly accurate technique to measure the trap alignment to the background magnetic field that can be used to align the multi-cell trap. Furthermore, the confined electron plasmas have been characterized and their confinement for different plasma lengths has been studied. A new mode of operation of the autoresonance technique has been demonstrated using a chirped rotating dipole field and has been found to be a reliable scheme to displace the plasma off-axis with minimal expansion. On the basis of these results and conclusions, we will proceed with the installation and operation of a prototype multi-cell test trap.

ACKNOWLEDGMENTS

This work was funded by the European Union's Horizon 2020 program (Grant No. 741322), the Deutsche Forschungsgemeinschaft (Grant Nos. Schw 401/23-1, Hu 978/15-1, and Sa 2788/2-1), and the U.S. DOE (Grant No. DE-SC0019271). The authors would especially like to thank Gerrit Marx for technical assistance and the rest of the APEX collaboration for their support.

AUTHOR DECLARATIONS

Conflict of Interest

The authors have no conflicts of interest to disclose.

DATA AVAILABILITY

The data that support the findings of this study are available from the corresponding author upon reasonable request.

REFERENCES

- C. Hugenschmidt, *Surf. Sci. Rep.* **71**, 547 (2016).
- C. Amole, G. B. Andresen, M. D. Ashkezari, M. Baquero-Ruiz, W. Bertsche, P. D. Bowe, E. Butler, A. Capra, P. T. Carpenter, C. L. Cesar *et al.*, *Nucl. Instrum. Methods Phys. Res., Sect. A* **735**, 319 (2014).
- W. A. Bertsche, *Philos. Trans. R. Soc., A* **376**, 20170265 (2018).

- ⁴T. Sunn Pedersen, J. R. Danielson, C. Hugenschmidt, G. Marx, X. Sarasola, F. Schauer, L. Schweikhard, C. M. Surko, and E. Winkler, *New J. Phys.* **14**, 035010 (2012).
- ⁵E. V. Stenson, H. Saitoh, J. Stanja, H. Niemann, U. Hergenbahn, T. Sunn Pedersen, G. H. Marx, L. Schweikhard, J. R. Danielson, C. M. Surko, and C. Hugenschmidt, *AIP Conf. Proc.* **1668**, 040004 (2015).
- ⁶M. R. Stoneking, T. Sunn Pedersen, P. Helander, H. Chen, U. Hergenbahn, E. V. Stenson, G. Fiksel, J. von der Linden, H. Saitoh, C. Surko *et al.*, *J. Plasma Phys.* **86**, 155860601 (2020).
- ⁷S. Niang, M. Charlton, J. J. Choi, M. Chung, P. Cladé, P. Comini, P. Crivelli, P. P. Crépin, O. Dalkarov, P. Debu *et al.*, *Acta Phys. Pol., A* **137**, 164 (2020).
- ⁸L. V. Jørgensen, M. Amoretti, G. Bonomi, P. D. Bowe, C. Canali, C. Carraro, C. L. Cesar, M. Charlton, M. Doser, A. Fontana *et al.*, *Phys. Rev. Lett.* **95**, 025002 (2005).
- ⁹D. W. Fitzakerley, M. C. George, E. A. Hessels, T. D. G. Skinner, C. H. Storry, M. Weel, G. Gabrielse, C. D. Hamley, N. Jones, K. Marable *et al.*, *J. Phys. B: At., Mol. Opt. Phys.* **49**, 064001 (2016).
- ¹⁰J. R. Danielson, D. H. E. Dubin, R. G. Greaves, and C. M. Surko, *Rev. Mod. Phys.* **87**, 247 (2015).
- ¹¹C. M. Surko and R. G. Greaves, *Radiat. Phys. Chem.* **68**, 419 (2003).
- ¹²J. R. Danielson, T. R. Weber, and C. M. Surko, *Phys. Plasmas* **13**, 123502 (2006).
- ¹³J. R. Danielson, N. C. Hurst, and C. M. Surko, *AIP Conf. Proc.* **1521**, 101 (2013).
- ¹⁴C. J. Baker, J. R. Danielson, N. C. Hurst, and C. M. Surko, *Phys. Plasmas* **22**, 022302 (2015).
- ¹⁵N. C. Hurst, J. R. Danielson, C. J. Baker, and C. M. Surko, *Phys. Plasmas* **26**, 013513 (2019).
- ¹⁶S. Robertson, Z. Sternovsky, and B. Walch, *Phys. Plasmas* **11**, 1753 (2004).
- ¹⁷M. R. Natisin, J. R. Danielson, and C. M. Surko, *Appl. Phys. Lett.* **108**, 024102 (2016).
- ¹⁸F. Ziegler, D. Beck, H. Brand, H. Hahn, G. Marx, and L. Schweikhard, *Nucl. Instrum. Methods Phys. Res., Sect. A* **679**, 1 (2012).
- ¹⁹G. Bettega, F. Cavaliere, M. Cavenago, A. Illiberi, R. Pozzoli, and M. Romé, *Phys. Plasmas* **14**, 042104 (2007).
- ²⁰J. H. Malmberg, C. F. Driscoll, B. Beck, D. L. Eggleston, J. Fajans, K. Fine, X. P. Huang, and A. W. Hyatt, *AIP Conf. Proc.* **175**, 28 (1988).
- ²¹F. Eckart, *Elektronenoptische Bildwandler und Röntgenbildverstärker* (Johann Ambrosius Barth Verlag, Leipzig, 1962).
- ²²E. V. Stenson, U. Hergenbahn, M. R. Stoneking, and T. Sunn Pedersen, *Phys. Rev. Lett.* **120**, 147401 (2018).
- ²³P. Steinbrunner, M.S. thesis, Universität Greifswald, 2020.
- ²⁴J. Aoki, Y. Kiwamoto, Y. Soga, and A. Sanpei, *Jpn. J. Appl. Phys., Part 1* **43**, 7777 (2004).
- ²⁵D. L. Eggleston, C. F. Driscoll, B. R. Beck, A. W. Hyatt, and J. H. Malmberg, *Phys. Fluids* **4**, 3432 (1992).
- ²⁶B. R. Beck, J. Fajans, and J. H. Malmberg, *Phys. Rev. Lett.* **68**, 317 (1992).
- ²⁷E. M. Hollmann, F. Anderegg, and C. F. Driscoll, *Phys. Plasmas* **7**, 2776 (2000).
- ²⁸J. R. Danielson and C. M. Surko, *Phys. Plasmas* **13**, 055706 (2006).
- ²⁹A. A. Kabantsev, K. A. Thompson, and C. F. Driscoll, *AIP Conf. Proc.* **1928**, 020008 (2018).
- ³⁰J. Fajans, E. Gilson, and L. Friedland, *Phys. Rev. Lett.* **82**, 4444 (1999).
- ³¹K. S. Fine, *Phys. Fluids* **4**, 3981 (1992).
- ³²K. S. Fine and C. F. Driscoll, *Phys. Plasmas* **5**, 601 (1998).
- ³³N. C. Hurst, J. R. Danielson, C. J. Baker, and C. M. Surko, *AIP Conf. Proc.* **1668**, 020003 (2015).
- ³⁴U. Wenzel, G. Schlisio, M. Mulsow, T. Sunn Pedersen, M. Singer, M. Marquardt, D. Pilopp, and N. Rüter, *Rev. Sci. Instrum.* **90**, 123507 (2019).